# Filamentation activates bacterial NLR-like antiviral protein

Yiqun Wang[1], Yuqing Tian[1], Xu Yang[1], Feng Yu[1] and Jianting Zheng[1,2*]
[1]State Key Laboratory of Microbial Metabolism, School of Life Sciences and Biotechnology, Shanghai Jiao Tong University, Shanghai 200240, China
[2]Joint International Research Laboratory of Metabolic & Developmental Sciences, Shanghai Jiao Tong University, Shanghai 200240, China
[*]Correspondence: Jianting Zheng, E-mail: jtzheng@sjtu.edu.cn

**Abstract**

Bacterial antiviral STANDs (Avs) are evolutionarily related to the nucleotide-binding leucine-rich repeat containing receptors (NLRs) widely distributed in immune systems across animals and plants. *Ef*Avs5, an Avs type 5 protein from *Escherichia fergusonii*, contains an N-terminal SIR2 effector domain, a nucleotide-binding oligomerization domain (NOD) and a C-terminal sensor domain, conferring protection against diverse phage invasions. Despite the established roles of SIR2 and STAND in prokaryotic and eukaryotic immunity, the mechanism underlying their collaboration remains unclear. Here we present cryo-EM structures of *Ef*Avs5 filaments, elucidating the mechanisms of dimerization, filamentation, filament clustering, ATP binding and $NAD^+$ hydrolysis, all of which are crucial for anti-phage defense. The SIR2 domains and NODs engage in the intra- and inter-dimer interaction to form an individual filament, while the outward C-terminal domains contribute to bundle formation. Filamentation potentially stabilizes the dimeric SIR2 configuration, thereby activating the NADase activity of *Ef*Avs5. *Ef*Avs5 is deficient in the ATPase activity, but elevated ATP concentrations can impede its NADase activity. Together, we uncover the filament assembly of Avs5 as a unique mechanism to switch enzyme activities and perform anti-phage defenses, emphasizing the conserved role of filamentation in immune signaling across diverse life forms.

**Keywords**

Sirtuin, signal transduction ATPases with numerous domains, bacterial defense system, $NAD^+$ hydrolysis, filament formation

**Keypoints**

- *Ef*Avs5 depletes $NAD^+$ for anti-phage defense.
- *Ef*Avs5 assembles as bundled filaments that can hydrolyze $NAD^+$.
- The SIR2 domain and NOD collaborate to form an individual filament.
- The building block of the filament is *Ef*Avs5 dimer.
- The activity of the *Ef*Avs5 complex is regulated by ATP.

## Introduction

Bacteria are in constant conflict with bacteriophages and develop diverse anti-phage defense systems of varying complexity[1-3]. The signal transduction ATPases with numerous domains (STAND) superfamily of P-loop NTPases, particularly the nucleotide-binding leucine-rich repeat containing receptors (NLRs) exemplified by animal inflammasomes and plant resistosomes[4-6], recognizes pathogens and triggers downstream inflammatory responses or apoptotic processes through

oligomerization, representing a conserved immune strategy in eukaryotes. Recently, this mechanism has also been discovered in the innate immunity of bacteria, known as antiviral STANDs (Avs)[3]. Avs proteins have a characteristic tripartite domain architecture: a central NTPase (alternatively called nucleotide-binding oligomerization domain, NOD); an extended C-terminal sensor with superstructure-forming repeats; and a variable N-terminal effector typically involved in cell death. Previous studies have revealed that Avs1-3 and Avs4 are activated by the phage terminases and portals, respectively, leading to the formation of tetramers that activate their N-terminal nucleases for antiviral defense[4].

Avs type 5 (Avs5) contains an N-terminal sirtuin (SIR2) effector and an unusual short C-terminal sensor domain, sometimes termed SIR2-STAND[3]. SIR2-mediated nicotinamide adenine dinucleotide hydrolase (NADase) activity represents a critical element in anti-phage immunity, triggering abortive infections via $NAD^+$ degradation and halting phage propagation, as exemplified by pAgo, Thoeris, DSR2, and the SIR2-HerA system[7-10]. In the Thoeris system, the signaling molecule 1''-3' gcADPR activates ThsA, which subsequently forms filaments and depletes $NAD^+$, ultimately triggering cell death and thereby preventing the spread of phage infection[11]. Another defense system DSR2 tetramerizes to form a supramolecular complex that specifically recognizes phage tail tube proteins, and leads to cellular $NAD^+$ depletion[12].

Despite reports on SIR2 and STAND roles in prokaryotic and eukaryotic immunity, the collaborative mechanism between them and the mechanisms underlying Avs5 activation and assembly remain obscure. Here, we present a biochemical and structural analysis of *Escherichia fergusonii* Avs5 (*Ef*Avs5), unveiling a unique mechanism of assembly-mediated activation by *Ef*Avs5. *Ef*Avs5 proteins form active filaments via SIR2 and NOD self-association, with sensor-mediated clustering enhancing their organization, allowing the $NAD^+$ depletion during phage infection. Moreover, the inactive NOD of *Ef*Avs5 requires ATP binding for its defensive role, whereas high ATP concentration impedes its NADase activity.

## Result

### 1. *Ef*Avs5 consumes $NAD^+$ to confer defense

Avs5 system is widely distributed across Gram-negative phyla, especially Pseudomonadota (Fig. S1). To define the molecular anti-phage defense mechanism of Avs5, we investigated a single protein Avs5 defense system from *E. fergusonii* phage-inducible chromosomal islands (PICI), named *Ef*Avs5 (Fig. 1A). *Ef*Avs5 is reported to defense against diverse *Escherichia coli*, *Salmonella* and *Klebsiella pneumoniae* phages[13]. We cultured *E. coli* cells expressing *Ef*Avs5 and found protection against T7 phages. The C terminal of *Ef*Avs5 is supposed to sense the phage invasion, while the SIR2 domain is suggested to be the effector depleting $NAD^+$. Indeed, a single amino acid substitution at NADase active site (N141A) was sufficient to abolish phage defense by the *Ef*Avs5 system, confirming that the NADase activity is essential for defense. Similarly, a point mutation disrupting the NOD active site, K379A in walker A or D426A in walker B, as well as a deletion of the C-terminal sensor domain, also abolished defense (Fig. 1A).

Growth curves of *E. coli* cultures in the presence of *Ef*Avs5 kept growing when subjected to the low (0.2) or medium (2) multiplicity of infection (MOI) in contrast to the cells expressing N141A mutant

89 or lacking *Ef*Avs5 (Fig. 1B). We measured the survival rate of cells infected with T7 and found that
90 *Ef*Avs5 increased cell survival after the first infection cycle (about 20 minutes) (Fig. 1C). Further
91 analysis showed that the phages amplified rapidly in the infected cells lacking *Ef*Avs5, but not in
92 the presence of *Ef*Avs5 (Fig. 1D). To investigate the effector's activity during immunity, we detected
93 the cellular $NAD^+$ content after infection with T7 phage. When subjected to the T7 phage infection,
94 compared to cells lacking *Ef*Avs5, the concentration of $NAD^+$ in the *Ef*Avs5-expressing cells was
95 declining rapidly after the first infection cycle, and began to rise in the second infection cycle (Fig.
96 1E). These results suggest that *Ef*Avs5 consumes $NAD^+$ to effectively prevent phage amplification
97 and leads to the population-level protection.
98
99 **2. Architecture of *Ef*Avs5 filament assembly**
100 To biochemically characterize the Avs5 system, we purified *Ef*Avs5 protein overexpressed in *E. coli*
101 BL21(DE3). The freshly isolated *Ef*Avs5 exists as soluble monomer (Fig. S2). Cryo-EM imaging of the
102 monomer *Ef*Avs5 revealed small particles. We tried to resolve the structure but only obtained two-
103 dimensional (2D) classes in poor resolution, possibly due to the flexibility (Fig. S3). However, the
104 purified *Ef*Avs5 becomes visibly cloudy after stored at 4°C or -80°C for two weeks. Negative staining
105 analysis of the suspension of *Ef*Avs5 confirmed that a significant fraction of the particles (>50%)
106 exhibited bundled 8-nm-wide fibrous assembly, and some of them extending up to ~400 nm in
107 length (Fig. 2A). Bundled fibrils can be connected parallelly or end-to-end and extend up to several
108 micrometers. Since previous studies show that the activated SIR2 or Toll/interleukin-1 receptor (TIR)
109 can assemble into helical filaments in Thoeris defense system, TIR-STING and TIR-SAVED effector,
110 respectively[11,14,15], we quantified the NADase activity of *Ef*Avs5. The freshly purified *Ef*Avs5 was
111 deficient in the NADase activity, but the filamentous *Ef*Avs5 displayed robust NADase activity (Fig.
112 2B).
113
114 To gain more insight into the filament formation, we determined the cryo-electron microscopy
115 (cryo-EM) structure of the active *Ef*Avs5. The final cryo-EM map was reconstructed using a total of
116 228,053 single particles and refined to a nominal resolution of 3.4 Å, with approximately 2.8 Å at
117 the center of filament and approximately 6.8 Å at the peripheral sensor lobes (Fig. 2C, Fig. S4 and
118 Table S1). The model was built with eight *Ef*Avs5 molecules assembled into a helical filament, and
119 extra densities suggest unlimited entries of both ends. The repeating building block of the filament
120 is *Ef*Avs5 dimer with a $C_2$ symmetry arranged into a regular helical structure with a helical twist of
121 84.531° and a helical rise of 48.600 Å (Fig. 2C). The filament is held together by 2 sets of inter-
122 subunit interactions, one between subunit n and n+3 and the other between subunit n+1 and n+2
123 (Fig. 2D). The *Ef*Avs5 proteins fold into five domains: a catalytic SIR2 domain, a core NOD, which
124 comprises the nucleotide-binding domain (NBD), helical domain (HD) and wing-helical domain
125 (WHD) and the C-terminal sensor domain (Fig. 1A and Fig. 2E). The core of the helix is composed
126 of the SIR2 and the NOD domain, whereas the C-terminal domain is pointing away and not involved
127 in the helical contacts (Fig. 2E).
128
129 **3. The dimerization of *Ef*Avs5**
130 In the *Ef*Avs5 filament, the individual dimeric unit adopts a $C_2$ symmetric conformation with a tight
131 interface (2329.2 $Å^2$ of buried surface area) (Fig. 3A). Within each *Ef*Avs5 dimer unit, abundant
132 contacts are observed between the WHD of one subunit and the NBD of its adjacent subunit,

133 encompassing salt bridges and hydrogen bonds, revealing an oligomerization pattern distinct from
134 other characterized active STAND ATPases, which primarily oligomerize through NBD-NBD and
135 WHD-WHD interactions (Fig. S5). The NBD of the n subunit interacts with the WHD of the n+1
136 subunit, comprising the salt bridge of the K461(n)- E589(n+1), K473(n)- E580(n+1), and the
137 hydrogen bonds of the T474(n)- Y583/R570(n+1) (Fig. 3B). Meanwhile, the WHD of the n subunit
138 interacts with the NBD of the n+1 subunit using slightly different residues, comprising the specific
139 contacts of the E580(n)- H362(n+1), and the hydrogen bonds of the Y583(n)- T474(n+1). The
140 dimeric interface is expanded by additional hydrogen bonds between its N-terminal SIR2 domains
141 (Fig. 3C). To probe the role of the dimer formation in *Ef*Avs5 activity, we generated mutants of the
142 dimeric interface. The substitutions of Y241 and T262 in SIR2 domain, H362A and K461 in NOD
143 abolished *Ef*Avs5 system antiviral defense, indicating that dimer formation is obligatory for *Ef*Avs5
144 anti-phage activity *in vivo* (Fig. 3D).
145
146 **4. SIR2- and NOD-dependent filamentation**
147 The *Ef*Avs5 structure features both SIR2 and NOD engaging in intra- and inter-dimer interactions,
148 resulting in two spirals: one dominated by SIR2, the other by NOD (Fig. 4A, B and E). The SIR2
149 domain within *Ef*Avs5 system exhibits a typical two-domain fold (Fig. 4D), resembling DSR2(PDB ID:
150 8WYB, rmsd of 1.160 Å for 74 aligned Cα atoms) and ThsA (PDB ID: 8BTO, rmsd of 1.247 Å for 84
151 aligned Cα atoms)[11,12], except for a longer α3 creating a broader substrate channel (Fig. S6). The
152 large domain (LD) has a Rossmann-fold core that is conserved among all the SIR2 proteins, while
153 the small domain (SD) lacks the three-stranded zinc-binding motif compared to human Sirt5[16].
154
155 The interface between SIR2 dimers is non-parallel to the helical axis (Fig. 4A), burying ~1218.8 $Å^2$
156 of surface area (Fig. 4B). SIR2 α4, α10 and α12 helices contribute to the intra-dimer interactions
157 (Fig. 3C), whereas the loop connecting β3 and β4 forms polar interactions and hydrogen bonds
158 with the loop between β4 and α9 of the adjacent SIR2, thereby constituting the inter-dimer
159 interactions and facilitating the assembly of *Ef*Avs5 filaments (Fig. 4C). Interestingly, despite the
160 similarity of the structure, the oligomerization mechanism of *Ef*Avs5-SIR2 is different from SIR2-
161 HerA, ThsA and DSR2 (Fig. S7). Identical to the intra-dimer interaction, the inter-dimer interactions
162 of NOD also mainly include the NBD-WHD contacts, but adopt a different mechanism (Fig. 4E). The
163 NBD interface of the n+1 molecule is predominantly negatively charged (I303, E307, E404),
164 complementing the positively charged interface of WHD domain of n+2 molecule (K552, H622,
165 K623) (Fig. 4F and G).
166
167 To probe the role of the filament formation in *Ef*Avs5 activity, we generated mutants D164A and
168 R185A of the interface between n and n+3 subunits, and double mutants I303A/E307A,
169 E404A/K552A and H622A/K623A of the interface between n+1 and n+2 subunits. These
170 substitutions abolished *Ef*Avs5 system antiviral defense, indicating that both SIR2-based and NOD-
171 based filament formation is obligatory for *Ef*Avs5 anti-phage activity *in vivo* (Fig. 3D).
172
173 **5. NADase catalytic pocket**
174 As expected, modeling of $NAD^+$ within the active site in the cryo-EM map of *Ef*Avs5 was not feasible
175 due to degradation by the active SIR2. Superimposing the SIR2 domain of *Ef*Avs5 onto both the
176 active and inactive conformations of ThsA reveals a comparable active pocket, situated within the

177 SIR2 dimer (Fig. 5A and Fig. 2D). Dimerization likely contributes to the stabilization of the active
178 pocket. In the case of ThsA and DSR2, the position of the loop above the active pocket decides to
179 block the $NAD^+$ access to the active site or enable $NAD^+$ binding, thus control the NADase activity
180 of SIR2[11,17]. However, in the *Ef*Avs5, the longer α3 pull this loop far away the active pocket (Fig. 5A
181 and Fig. S6), indicating a different activation mechanism adopted by *Ef*Avs5. In the *Ef*Avs5-$NAD^+$
182 predicted model, the A41, T140, N141, Y142, N180, Y202, S233 in the pocket interact with $NAD^+$,
183 creating an ideal condition for the reaction (Fig. 5B). The Y202 is also involved in SIR2-based
184 dimerization. These residues are highly conserved in the bacterial SIR2 proteins, except the
185 substitution of an Asn residue with His at residue 180 in *Ef*Avs5 (Fig. S8).
186
187 **6. ATP inhibits the NADase activity of the *Ef*Avs5 system**
188 The NOD of *Ef*Avs5 is an $AAA^+$ ATPase, belongs to a novel STAND NTPase 3 family found in bacterial
189 conflict systems and in metazoan TRADD-N associated counter-invader proteins[18]. The structural
190 comparison in Dali server[19] suggested that *Ef*Avs5's NOD is most similar to the plant NLR RPP1(PDB
191 ID: 7CRC, rmsd of 1.160 Å for 56 aligned Cα atoms) and cell death protein 4 in *Caenorhabditis*
192 *elegans* (PDB ID: 4M9S, rmsd of 1.239 Å for 45 aligned Cα atoms). Notably, we found that *Ef*Avs5 is
193 an inactive ATPase either in the monomer or filament assembly (Fig. 5C). Consistently, the cryo-EM
194 map allows modelling of ATP molecules in each NOD active site (Fig. 5D), although we did not add
195 additional ATP during the sample preparation. In the structure, ATP molecules are buried in the
196 active pocket between NBD and WHD (Fig. 5E), with an adjacent magnesium ion coordinated by
197 the canonical Walker A and B motif (Fig. 5F). The K379 and S380 in Walker A form hydrogen bonds
198 with the oxygens of the phosphate groups, determining the orientation of ATP. Meanwhile, the
199 acidic D426 in Walker B binds to the $Mg^{2+}$. The recognition of the γ-phosphate group of ATP in the
200 ZAR1 resistosome and Apaf-1 apoptosome is facilitated by an arginine residue in the conserved
201 'TT/SR' motif, which is crucial for their activation and preserved as 'TTR' and R453 in *Ef*Avs5[20,21].
202 The I351 forms hydrogen bonds with the N6 atoms of the adenine ring (Fig. 5F). The region
203 spanning residues 300-366, sometimes described as the fish-specific NACHT-associated (FISNA)
204 domain, resembles the active state of NLRP3 (PDB ID:8EJ4), triggering conformational alterations
205 and oligomerization[22]. The accurate positioning of ATP is crucial for the functionality of the *Ef*Avs5
206 system, as evidenced by the phage plaque assays with WalkerA/B mutants (Fig. 1A). The deficiency
207 of ATP hydrolysis probably results from its WHD domain's unique conformations near the active
208 site, particularly the hydrogen bonding between R537 and the ATP phosphate, contrasting with
209 other active STAND ATPases (Fig. 5F and Fig. S9).
210
211 Based on the role of ATPase in sustaining *Ef*Avs5's activity *in vivo*, we investigated the potential
212 impact of ATP on $NAD^+$ hydrolysis. Our findings revealed that low ATP concentrations (0.05 and 0.5
213 mM) had negligible effects, whereas 5 mM ATP significantly reduced *Ef*Avs5's NADase activity by
214 40% (Fig. S10). Notably, GTP and dGTP also effectively inhibited NADase activity, while other
215 NTPs/dNTPs showed minimal effects, except for a slight inhibition by UTP (Fig. 5G). These results
216 indicate that specific NTP/dNTP and its concentration can inhibit *Ef*Avs5's NADase activities.
217
218 **7. Filamentous cluster formation mediates *Ef*Avs5 anti-phage activity**
219 *Ef*Avs5 filaments are organized into higher-order structures, forming bundles or three-dimensional
220 networks (Fig. 2A). Although density maps of the filament bundle were not available, interactions

221 between filaments were observed during 2D classification in cryo-EM analysis (Fig. 6A), in which
222 the *Ef*Avs5 exhibits an end-to-end linkage between dimers from adjacent filaments (Fig. 6B).
223 Notably, the C-terminal sensor possesses a predominantly positive charge, which complements the
224 negatively charged interface of the N-terminal SIR2 domain residing in adjacent filaments (Figure
225 6C). These interactions would enable the *Ef*Avs5 filament to extend in four distinct directions,
226 thereby promoting the formation of parallel bundles (Figure 6D). The C-terminus of *Ef*Avs5 does
227 not participate in the formation of the individual filament but may play a crucial role in filament
228 clustering. Deletion of the entire C-terminal sensor abolished *Ef*Avs5 activity (Fig. 1A). Further
229 analysis confirmed that deletion of C-terminal six positively charged amino acids similarly
230 abolished *Ef*Avs5's resistance to phage invasion, as well as the mutations of D79A, E85A and K792A
231 at interaction interfaces (Fig. 6E). These results indicated that filament clustering may be essential
232 for the anti-phage function of *Ef*Avs5.
233
234 **Discussion**
235 In this study, we determined the cryo-EM structures of the *Ef*Avs5 and found that *Ef*Avs5 assembles
236 into bundled filaments for NADase activity and anti-phage defense. We propose the following
237 model for *Ef*Avs5 (Fig. 6F). Without phage infection, *Ef*Avs5 adopts an inactive, monomeric
238 conformation in cells. Phage infection triggers *Ef*Avs5 to form filament bundles, in which SIR2
239 adopts a dimeric active state. This active state enables *Ef*Avs5 to rapidly degrade $NAD^+$, leading to
240 an abortive infection that prevents propagation of phage through a population of cells.
241
242 The *Ef*Avs5 structure displays a filament assembly distinct from the characterized SIR2-containing
243 defense systems and STAND proteins, underlining the universal yet diverse nature of filamentation
244 as an antiviral mechanism across prokaryotic and eukaryotic immune systems. The *Ef*Avs5 filament
245 is formed by *Ef*Avs5 dimers with a C2 symmetry arranged into a high-order complex, involving
246 comprehensive SIR2-SIR2 and NBD-WHD interactions. In SIR2-APAZ/Ago, DSR2, SIR2-HerA and
247 Thoeris system, SIR2 domains function as monomers, tetramers (dimer of dimers), dodecamers
248 (hexamer of dimers) and filament (spiral of tetramers), respectively[7-10]. Compared with the SIR2-
249 based filamentation in ThsA, the NOD and SIR2 domain work together to facilitate filament
250 formation in *Ef*Avs5, highlighting their independent yet complementary roles in the assembly
251 process. Moreover, to the best of our knowledge, *Ef*Avs5 represents the first STAND family protein
252 reported to assemble into functional filaments. The activation of STAND family proteins typically
253 involves oligomerization, which includes tetramers (*Se*Avs3, *Ec*Avs4, and plant TIR-NLRs),
254 pentamers (plant ZAR1), heptamers (animal apoptosome Apaf-1) or octamers (Drosophila dark
255 apoptosome)[4,21,23-25]. Notably, *Solanum lycopersicum* NRC2 (*Sl*NRC2) was recently found to form
256 filaments at elevated concentrations, but adopt an inactive conformation to avoid self-activation.
257 Distinct from *Ef*Avs5, the *Sl*NRC2 filament consists of three identical protofilaments, which contain
258 copies of tetramers[26].
259
260 The activation observed in this study appears to be correlated with the accumulation of *Ef*Avs5
261 proteins, mirroring previous findings in plants where concentration-dependent hypersensitive
262 response cell death was mediated by the plant NLR protein[27,28]. Considering its genomic
263 localization on a PICI, intracellular expression of *Ef*Avs5 may be tightly regulated to avoid
264 unnecessary activity. The phage signals activating *Ef*Avs5 remain unclear. We speculated that the

activation of *Ef*Avs5 upon phage infection may involve binding of an as-yet-unidentified protein or compound; alternatively, it may be a response to changes in substrate concentration. Firstly, *Ef*Avs5 may interact with either phage-derived proteins, akin to the DSR2 system[9], or host-derived proteins, such as that involved in the bNACHT25 system[29], leading to the activation of filament formation and enzymatic activity. However, our attempt to identify potential activators through screening of escape phages was unsuccessful. Secondly, as suggested by the finding that the binding of the TIR substrates $NAD^+$ and ATP induces phase separation and activation of TIR *in vitro*[30], one of the potential activation mechanisms of *Ef*Avs5 may be the substrate-based response.

Above all, our structural and biochemical findings offer insights into the molecular mechanism of Avs5 bacterial immune system, highlighting the conservation of filamentation as a key regulatory mechanism governing antiviral defense across prokaryotes and metazoans.

**Limitations of the study**

Our findings elucidate the fundamental mechanisms underlying *Ef*Avs5 function, yet the activation signals associated with phage infection remain elusive and warrant further investigation. Apart from biochemical assays on mutants, our results lack direct evidence of *Ef*Avs5 forming fibrillar clusters *in vivo*. Additionally, we propose that ATP intricately modulates *Ef*Avs5 activity, but the underlying molecular mechanisms require detailed clarification.

**Acknowledgements**

This work was supported by National Natural Science Foundation of China (32370071, 32070040), National Key Research and Development Program of China (2020YFA0907900, 2019YFA0905400). We thank the staff members of the Electron Microscopy System at the National Facility for Protein Science in Shanghai (NFPS), Shanghai Advanced Research Institute, Chinese Academy of Sciences, China for providing technical support and assistance in data collection. We thank Jing Liu, Xinqiu Guo and Mengyu Yan at the Instrument Analysis Center (IAC) of Shanghai Jiao Tong University for providing assistance in data collection.

**Author contributions**

J.Z. and Y.W. designed the experiments and analyzed data.
Y.W. and Y.T. performed biochemical assays.
Y.W. and X.Y. conducted cryo-EM data collection.
Y.W. conducted image processing, atomic model, building and refinement and structural analyses.
Y.W. and Y.F performed bioinformatics analysis.
Y.W. and J.Z. wrote the manuscript.

**Declaration of interests**

The authors declare no competing interests.

**Data availability**

The atomic coordinates have been deposited in the Protein Data Bank under accession codes 9JAP. The corresponding maps have been deposited in the Electron Microscopy Data Bank under the accession number EMD-61299. Original data for biochemical assays and uncropped gels were

309 deposited to Figshare.
310
311 **Supplemental information**
312 Document S1. Figures S1–S10 and Table S1-S2
313
314 **Methods**
315 **Plasmid construction**
316 DNA fragments encoding *Ef*Avs5 from *Escherichia fergusonii* PICI EfCIRHB19-C05 (QML19490.1)
317 were synthesized and inserted into the expressing plasmids pET28a with N-terminal $His_6$-tag by
318 Universe Gene Technology (Tianjin). The DNA fragments encoding *Ef*Avs5 was subcloned into the
319 pBAD33 vector for phage infection assays. Plasmids carrying *Ef*Avs5 mutants were constructed
320 using site-directed mutagenesis. Primers used are listed in Table S2.
321
322 **Protein expression and purification**
323 The vector pET28a-*Ef*Avs5 was transformed into *E. coli* BL21(DE3). Induction of expression was
324 achieved by adding 0.3 mM isopropyl-β-D-thiogalactopyranoside (IPTG) and incubated for 16 h at
325 16°C and 220 rpm. The cells were then harvested and resuspended in buffer A (50 mM Tris, pH 8.0,
326 500 mM NaCl, 5 mM $MgCl_2$, 10% glycerol, 1 mM β-mercaptoethanol and 5 mM imidazole). After
327 purification by nickel-NTA, the eluate was further loaded onto a size exclusion chromatography
328 column (SEC) (Superose 6, Cytiva) equilibrated with buffer B (20 mM Tris, pH 8.0, 150 mM NaCl, 5
329 mM $MgCl_2$, 5% glycerol) and the purified proteins were stored at −80 °C.
330
331 **Plaque assays**
332 *E. coli* MG1655 possessing pBAD33- *Ef*Avs5, its mutants or an empty vector(pBAD33) were grown
333 at 37℃ in LB medium. When the $OD_{600}$ reached 0.4, cells were induced with 0.5% L-arabinose for
334 1 hour. Then, 150 µL of the culture was mixed with 3 mL LB containing 0.8% low-melting agarose
335 （with 0.5% L-arabinose added）, and the mixture was poured into LB agar base layer in the 9 cm
336 petri dish. Ten-fold dilutions of high-titers(>$10^8$pfu/mL) of phage T7 were spotted onto the agar
337 and incubated overnight at 37 ℃. The next day, plates were photographed with blue-white light
338 reflection in the dark box.
339
340 **Phage-infection in liquid medium**
341 *E. coli* MG1655 possessing pBAD33- *Ef*Avs5, its mutant(N141A) or an empty vector(pBAD33) were
342 grown until the $OD_{600}$ reached 0.4. These cultures were then induced with 0.5% L-arabinose for 1
343 hour, and diluted in LB containing 0.5% L-arabinose to an OD of ~0.1. Phage T7 was added to the
344 culture at final MOI of 0.02, 0.2, 2, and 10. Subsequently, 200 µL of the diluted culture was placed
345 into the wells of a 96-well plate. During shaking, the $OD_{600}$ was measured every 5 minutes at 37℃
346 for 6 hours.
347
348 **Cell survival assays**
349 Overnight cultures of *E. coli* MG1655, either containing the plasmid pBAD33-*Ef*Avs5 or an empty
350 vector, were diluted 1:100 into fresh LB medium. These cultures were grown at 37°C with the
351 addition of 0.5% L-arabinose until they reached an $OD_{600}$ of 0.4. Subsequently, the cells were
352 harvested by centrifugation, washed with LB, and resuspended to an $OD_{600}$ of 0.2. To each sample,

353 phage T7 was added at an MOI of 5, while control samples were left without phage addition.
354 Following a 20-minute adsorption period, serial 10-fold dilutions of each sample were plated onto
355 LB agar, and the plates were incubated overnight at 37°C. The cell survival rate was determined by
356 comparing the CFU obtained from the samples with phage T7 addition to the CFU obtained from
357 the control samples without phage, expressed as a percentage.
358
359 **Phage burst size measurements**
360 Overnight cultures of *E. coli* MG1655 harboring either the pBAD33-*Ef*Avs5 plasmid or an empty
361 vector were diluted 1:100 in LB medium supplemented with 0.5% L-arabinose. These diluted
362 cultures were then grown at 37°C until they reached an $OD_{600}$ of 0.4. Subsequently, T7 phages were
363 introduced to the cultures at an MOI of 0.1, and the infection process was allowed to proceed at
364 37°C. To establish a baseline for the initial phage titer, an equal volume of phage was added to LB
365 media and used as the reference for time 0 of infection. After infection for 20, 40, and 60 minutes
366 at 37°C, which represent approximately one, two, and three cycles of T7 phage replication,
367 respectively, 0.5 mL samples of the culture were withdrawn. These samples were centrifuged at
368 5000 rpm for 7 minutes and the supernatants were filtered through a 0.22 μm filter. The titer of
369 the T7 phages present in the filtered supernatants was determined by a plaque assay using *E. coli*
370 MG1655 as the host.
371
372 **NAD(H) degradation measurements**
373 NAD(H) concentrations were measured using the Innochem Coenzyme I NAD(H) Content Assay Kit
374 (WST colorimetry), following the manufacturer's instructions. Briefly, overnight cultures were
375 diluted 1:100 in 50 mL LB with 0.5% L-arabinose, grown to $OD_{600}$ of 0.4, and infected with T7 phage
376 at an MOI of 2. At indicated times, 1 mL cultures were centrifuged, resuspended in acidic extract,
377 sonicated, boiled, rapid cooled, and centrifuged. Supernatant was neutralized with alkaline extract.
378 50 μL of the neutralized supernatant was combined sequentially with 250 μL of Reagent 1, 75 μL
379 of Reagent 2, 150 μL of Reagent 3, and 35 μL of Reagent 4 in the determination tube. After a 1-
380 hour dark reaction, Reagent 5 was added to the mixture. In the control tube, Reagent 5 was added
381 first, followed by the supernatant, maintaining identical steps thereafter. Absorbance was
382 measured at 450 nm, and NAD(H) levels were calculated using a standard curve and normalized to
383 the amount of NAD(H) present in an equivalent volume of sample with an $OD_{600}$ of 0.1 to allow for
384 accurate comparisons between samples.
385
386 **Negative staining analysis**
387 The *Ef*Avs5 sample was directly applied to a glow-discharged 400-mesh Cu grid (Beijing
388 ZhongJingKeYi Technology) for 30 s. After side blotting, the grid was immediately stained with 2%
389 uranyl formate and then blotted again from the side. Staining was repeated twice with a 30 s
390 incubation with uranyl formate in the final staining step. EM images were collected on a Talos
391 F200C G2 at a nominal magnification of 52,000× and at a defocus of about 5 μm.
392
393 **Cryo-EM grid preparation and data acquisition**
394 3.5 μL of the *Ef*Avs5 samples were added to freshly glow-discharged Quantifoil R1.2/1.3 Cu 300
395 mesh grids. In a Vitrobot (FEI, Inc.), grids were plunge-frozen in liquid ethane after being blotted
396 for 2 s at 16°C with 100% chamber humidity. The grids were imaged using EPU on Titan Krios 300

397 kV microscopes with a K3 detector. Totally 4318 movies were collected under the defocus ranged
398 from −0.8 to −1.6 μm, and the magnification was 81k in super-resolution mode. 32 frames per
399 movie were collected with a total dose of 40 $e^-/Å^2$.
400
401 **Cryo-EM data processing and model building**
402 The cryo-EM data was processed using CryoSPARC suite v4.5.3[31]. After motion correction, patch
403 CTF estimation and manual exposure curation, 1425 movies were selected. The first set of particles
404 was picked using a filament tracer, and after two-dimensional (2D) classification, good templates
405 were selected for template picking. A total of 1,392,237 particles were picked using a template
406 picker and extracted (box size 360 pixels) from 1,425 accepted micrographs (Fig. S4). Two rounds
407 of 2D classification were conducted and 364,551 particles were picked and used for ab-initio
408 reconstruction (three classes). The largest 3D class (228,053 particles, 62.6%) was selected and
409 refined by homogeneous refinement, non-uniform refinement and CTF refinement to give the final
410 map (global resolution, 3.44 Å). Helical parameters (helical twist and helical rise) were determined
411 by helical refinement job. The initial model of *Ef*Avs5 wes generated by AlphaFold[32]. The model of
412 ATP was built in Coot[33]. The models of *Ef*Avs5 were fitted into the cryo-EM density maps using
413 ChimeraX[34]. The model was refined in Coot and Phenix with secondary structure, rotamer and
414 Ramachandran restraints[35]. The Map versus Model FSCs was generated by Phenix (Fig. S4). The
415 statistics of cryo-EM data processing and refinement were listed in Table S1.
416
417 ***In vitro* NADase activity**
418 The *Ef*Avs5 NADase activity was evaluated through an $εNAD^+$-based fluorescence assay, wherein
419 the enzymatic cleavage of the nicotinamide glycosidic bond in $εNAD^+$ results in the formation of
420 εADPR, which subsequently emits a fluorescent signal. In a 96-well black flat-bottom plate, 100 μL
421 reaction mixtures were prepared, each containing 50 μM of $εNAD^+$ (Sigma catalogue No. N2630)
422 and 0.5 μM *Ef*Avs5 proteins in reaction buffer (20 mM Tris, pH 8.0, 150 mM NaCl, and 5% glycerol,
423 with and without the addition of nucleotides). A mixture containing only the reaction buffer and
424 $εNAD^+$ was used as a control. The reactions were then loaded into a BioTek Synergy H1 microplate
425 reader, and fluorescence intensities were recorded at 37°C every 20 seconds for 15 minutes,
426 employing excitation and emission wavelengths of 310 nm and 410 nm, respectively. All
427 experiments were conducted in triplicate to ensure reproducibility.
428
429 **ATPase activity**
430 ATPase activities were evaluated by using Malachite Green Phosphate Detection Kit (Beyotime).
431 Each 200 μL reaction mixture consisted of 5μM *Ef*Avs5 proteins in a reaction buffer (20 mM Tris,
432 pH 8.0, 150 mM NaCl, 5 mM $MgCl_2$ and 0.5 mM ATP). A mixture without the addition of *Ef*Avs5
433 proteins served as a control. Following a 30-minute incubation at 37°C, 70 μL of color reagent was
434 added and the mixture was further incubated for another 30 minutes. Subsequently, the
435 absorbance at 620 nm was measured using a multi-detection microplate reader (Tecan Spark).
436 Phosphate levels were then calculated using a standard curve generated with phosphate standards.
437 All experiments were conducted in triplicate to ensure reproducibility.
438
439 **Phylogenetic analysis of Avs5 systems**
440 The coding sequence of Avs5 was acquired from two sources: firstly, by utilizing the defense finder

441 tool to scan through all bacterial and archaeal genomes housed in the IMG (Integrated Microbial
442 Genomes & Microbiomes) database from November 2023, aiming to identify proteins that encode
443 the Avs5 system[36]; secondly, by leveraging the Foldseek search server to discover proteins
444 (leveraging AlphaFold/UniProt50, ensuring a coverage exceeding 80%) that exhibited a high degree
445 of structural similarity to Avs5[37]. To eliminate redundancy, MMseqs was employed with the
446 specified parameters '–min-seq-id 0.90' and '-c 0.8', resulting in 263 filtered sequences[38]. These
447 sequences were subsequently aligned using MAFFT, with the parameters set to '--maxiterate 1000
448 –globalpair' for optimal alignment[39]. Following alignment, trimAl was applied to refine the
449 alignment by trimming unnecessary regions[40]. The phylogenetic tree was then constructed using
450 IQ-TREE, incorporating the parameters '-nstop 500 -bb 1000 -m LG+F+I+G4' for enhanced accuracy
451 and robustness[41]. Finally, iTOL was utilized for the visualization and annotation of the phylogenetic
452 tree[42].
453
454
455 **References**


456 1 Millman, A. *et al.* An expanded arsenal of immune systems that protect bacteria from phages.
457 *Cell Host & Microbe* **30**, 1556-1569.e1555 (2022). https://doi.org:10.1016/j.chom.2022.09.017
458 2 Vassallo, C. N., Doering, C. R., Littlehale, M. L., Teodoro, G. I. C. & Laub, M. T. A functional
459 selection reveals previously undetected anti-phage defence systems in the E. coli pangenome.
460 *Nature Microbiology* **7**, 1568-1579 (2022). https://doi.org:10.1038/s41564-022-01219-4
461 3 Gao, L. *et al.* Diverse enzymatic activities mediate antiviral immunity in prokaryotes. *Science*
462 **369**, 1077-1084 (2020). https://doi.org:10.1126/science.aba0372
463 4 Gao, L. A. *et al.* Prokaryotic innate immunity through pattern recognition of conserved viral
464 proteins. *Science* **377** (2022). https://doi.org:10.1126/science.abm4096
465 5 Huang, S. *et al.* NLR signaling in plants: from resistosomes to second messengers. *Trends in*
466 *Biochemical Sciences* **48**, 776-787 (2023). https://doi.org:10.1016/j.tibs.2023.06.002
467 6 Mitchell, P. S., Sandstrom, A. & Vance, R. E. The NLRP1 inflammasome: new mechanistic
468 insights and unresolved mysteries. *Curr Opin Immunol* **60**, 37-45 (2019).
469 https://doi.org:10.1016/j.coi.2019.04.015
470 7 Koopal, B. *et al.* Short prokaryotic Argonaute systems trigger cell death upon detection of
471 invading DNA. *Cell* **185**, 1471-1486.e1419 (2022). https://doi.org:10.1016/j.cell.2022.03.012
472 8 Ka, D., Oh, H., Park, E., Kim, J.-H. & Bae, E. Structural and functional evidence of bacterial
473 antiphage protection by Thoeris defense system via NAD+ degradation. *Nature*
474 *Communications* **11** (2020). https://doi.org:10.1038/s41467-020-16703-w
475 9 Garb, J. *et al.* Multiple phage resistance systems inhibit infection via SIR2-dependent NAD+
476 depletion. *Nature Microbiology* **7**, 1849-1856 (2022). https://doi.org:10.1038/s41564-022-
477 01207-8
478 10 Tang, D. *et al.* Multiple enzymatic activities of a Sir2-HerA system cooperate for anti-phage
479 defense. *Molecular Cell* **83**, 4600-4613.e4606 (2023).
480 https://doi.org:10.1016/j.molcel.2023.11.010
481 11 Tamulaitiene, G. *et al.* Activation of Thoeris antiviral system via SIR2 effector filament assembly.
482 *Nature* (2024). https://doi.org:10.1038/s41586-024-07092-x
483 12 Yang, X., Wang, Y. & Zheng, J. Structural insights into autoinhibition and activation of defense-
484 associated sirtuin protein. *Int J Biol Macromol* **277**, 134145 (2024).

485 https://doi.org:10.1016/j.ijbiomac.2024.134145
486 13 Fillol-Salom, A. *et al.* Bacteriophages benefit from mobilizing pathogenicity islands encoding
487 immune systems against competitors. *Cell* **185**, 3248-3262.e3220 (2022).
488 https://doi.org:10.1016/j.cell.2022.07.014
489 14 Morehouse, B. R. *et al.* Cryo-EM structure of an active bacterial TIR–STING filament complex.
490 *Nature* **608**, 803-807 (2022). https://doi.org:10.1038/s41586-022-04999-1
491 15 Hogrel, G. *et al.* Cyclic nucleotide-induced helical structure activates a TIR immune effector.
492 *Nature* **608**, 808-812 (2022). https://doi.org:10.1038/s41586-022-05070-9
493 16 Du, J. *et al.* Sirt5 is a NAD-dependent protein lysine demalonylase and desuccinylase. *Science*
494 **334**, 806-809 (2011). https://doi.org:10.1126/science.1207861
495 17 Yin, H. *et al.* Insights into the modulation of bacterial NADase activity by phage proteins. *Nature*
496 *Communications* **15** (2024). https://doi.org:10.1038/s41467-024-47030-z
497 18 Kaur, G., Iyer, L. M., Burroughs, A. M. & Aravind, L. Bacterial death and TRADD-N domains help
498 define novel apoptosis and immunity mechanisms shared by prokaryotes and metazoans. *Elife*
499 **10** (2021). https://doi.org:10.7554/eLife.70394
500 19 Holm, L. Dali server: structural unification of protein families. *Nucleic Acids Res* **50**, W210-w215
501 (2022). https://doi.org:10.1093/nar/gkac387
502 20 Wang, J. *et al.* Reconstitution and structure of a plant NLR resistosome conferring immunity.
503 *Science* **364** (2019). https://doi.org:10.1126/science.aav5870
504 21 Zhou, M. *et al.* Atomic structure of the apoptosome: mechanism of cytochrome c- and dATP-
505 mediated activation of Apaf-1. *Genes Dev* **29**, 2349-2361 (2015).
506 https://doi.org:10.1101/gad.272278.115
507 22 Xiao, L., Magupalli, V. G. & Wu, H. Cryo-EM structures of the active NLRP3 inflammasome disc.
508 *Nature* **613**, 595-600 (2023). https://doi.org:10.1038/s41586-022-05570-8
509 23 Ma, S. *et al.* Direct pathogen-induced assembly of an NLR immune receptor complex to form a
510 holoenzyme. *Science* **370** (2020). https://doi.org:10.1126/science.abe3069
511 24 Wang, J. *et al.* Reconstitution and structure of a plant NLR resistosome conferring immunity.
512 *Science* **364** (2019). https://doi.org:10.1126/science.aav5870
513 25 Pang, Y. *et al.* Structure of the apoptosome: mechanistic insights into activation of an initiator
514 caspase from Drosophila. *Genes Dev* **29**, 277-287 (2015).
515 https://doi.org:10.1101/gad.255877.114
516 26 Ma, S. *et al.* Oligomerization-mediated autoinhibition and cofactor binding of a plant NLR.
517 *Nature* **632**, 869-876 (2024). https://doi.org:10.1038/s41586-024-07668-7
518 27 Zhang, Y., Dorey, S., Swiderski, M. & Jones, J. D. Expression of RPS4 in tobacco induces an
519 AvrRps4-independent HR that requires EDS1, SGT1 and HSP90. *Plant J* **40**, 213-224 (2004).
520 https://doi.org:10.1111/j.1365-313X.2004.02201.x
521 28 Horsefield, S. *et al.* NAD(+) cleavage activity by animal and plant TIR domains in cell death
522 pathways. *Science* **365**, 793-799 (2019). https://doi.org:10.1126/science.aax1911
523 29 Conte, A. N. *et al.* (2024). https://doi.org:10.1101/2024.06.04.597415
524 30 Song, W. *et al.* Substrate-induced condensation activates plant TIR domain proteins. *Nature*
525 **627**, 847-853 (2024). https://doi.org:10.1038/s41586-024-07183-9
526 31 Punjani, A., Rubinstein, J. L., Fleet, D. J. & Brubaker, M. A. cryoSPARC: algorithms for rapid
527 unsupervised cryo-EM structure determination. *Nat Methods* **14**, 290-296 (2017).
528 https://doi.org:10.1038/nmeth.4169

32 Jumper, J. *et al.* Highly accurate protein structure prediction with AlphaFold. *Nature* **596**, 583-589 (2021). https://doi.org:10.1038/s41586-021-03819-2

33 Casanal, A., Lohkamp, B. & Emsley, P. Current developments in Coot for macromolecular model building of Electron Cryo-microscopy and Crystallographic Data. *Protein Sci* **29**, 1069-1078 (2020). https://doi.org:10.1002/pro.3791

34 Pettersen, E. F. *et al.* UCSF ChimeraX: Structure visualization for researchers, educators, and developers. *Protein Sci* **30**, 70-82 (2021). https://doi.org:10.1002/pro.3943

35 Liebschner, D. *et al.* Macromolecular structure determination using X-rays, neutrons and electrons: recent developments in Phenix. *Acta Crystallogr D Struct Biol* **75**, 861-877 (2019). https://doi.org:10.1107/S2059798319011471

36 Tesson, F. *et al.* Systematic and quantitative view of the antiviral arsenal of prokaryotes. *Nat Commun* **13**, 2561 (2022). https://doi.org:10.1038/s41467-022-30269-9

37 van Kempen, M. *et al.* Fast and accurate protein structure search with Foldseek. *Nat Biotechnol* **42**, 243-246 (2024). https://doi.org:10.1038/s41587-023-01773-0

38 Steinegger, M. & Söding, J. MMseqs2 enables sensitive protein sequence searching for the analysis of massive data sets. *Nat Biotechnol* **35**, 1026-1028 (2017). https://doi.org:10.1038/nbt.3988

39 Katoh, K., Rozewicki, J. & Yamada, K. D. MAFFT online service: multiple sequence alignment, interactive sequence choice and visualization. *Brief Bioinform* **20**, 1160-1166 (2019). https://doi.org:10.1093/bib/bbx108

40 Capella-Gutiérrez, S., Silla-Martínez, J. M. & Gabaldón, T. trimAl: a tool for automated alignment trimming in large-scale phylogenetic analyses. *Bioinformatics* **25**, 1972-1973 (2009). https://doi.org:10.1093/bioinformatics/btp348

41 Nguyen, L. T., Schmidt, H. A., von Haeseler, A. & Minh, B. Q. IQ-TREE: a fast and effective stochastic algorithm for estimating maximum-likelihood phylogenies. *Mol Biol Evol* **32**, 268-274 (2015). https://doi.org:10.1093/molbev/msu300

42 Letunic, I. & Bork, P. Interactive Tree Of Life (iTOL) v5: an online tool for phylogenetic tree display and annotation. *Nucleic Acids Res* **49**, W293-w296 (2021). https://doi.org:10.1093/nar/gkab301

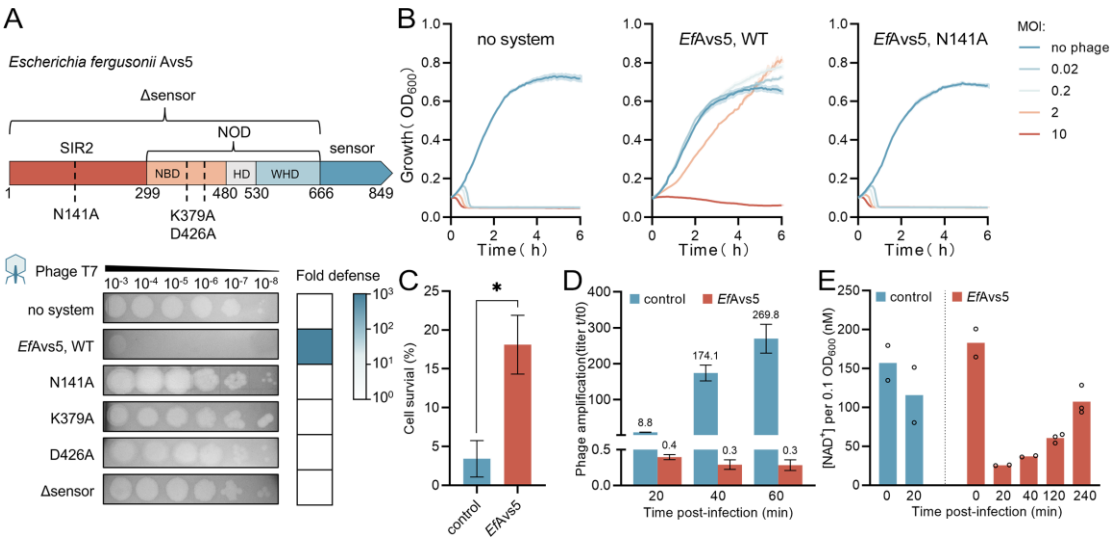


**Fig. 1. *Ef*Avs5 consumes NAD⁺ to confer defense.**

(**A**) Domain organization of the *Ef*Avs5 protein from *Escherichia fergusonii* and efficiency of plating of T7 phages infecting *E. coli* expressing *Ef*Avs5 or an empty vector. Data are representative images of n=3 biological replicates. Mutations used are indicated below the domain organization. NBD, nucleotide-binding domain; HD, helical domain; WHD, wing-helical domain; NOD, nucleotide-binding oligomerization domain. (**B**) Infection time courses for liquid cultures of *E. coli*, with *Ef*Avs5, *Ef*Avs5 N141A or empty vector, infected at different multiplicities of infection (MOI) of phage T7. Data represent the mean of three replicates and shaded regions represent the standard error of the mean (SEM). (**C**) Survival of *E. coli* cells expressing either the *Ef*Avs5 or empty vector as a control infected at an MOI of 5 with T7 for 20 minutes. Data represent the mean of three replicates and error bars represent the SEM. (**D**) Titer of T7 phage propagated on *E. coli* cells expressing either the *Ef*Avs5 or empty vector as a control infected at an MOI of 0.1 with T7. Data represent the titer of T7 measured in PFU/mL after indicated time from initial infection, divided by the original phage titer prior to infection. Data represent the mean of three replicates and error bars represent the SEM. (**E**) Measurement of $NAD^+$ concentration in *E. coli* expressing *Ef*Avs5 or empty vector as a control at the indicated time points after infection with phage T7 at an MOI of 2, normalized to an $OD_{600}$ of 0.1. The control group underwent near-complete lysis after 20 minutes of infection, precluding the quantification of $NAD^+$ content. Data represent the mean of two or three replicates and error bars represent the SEM.

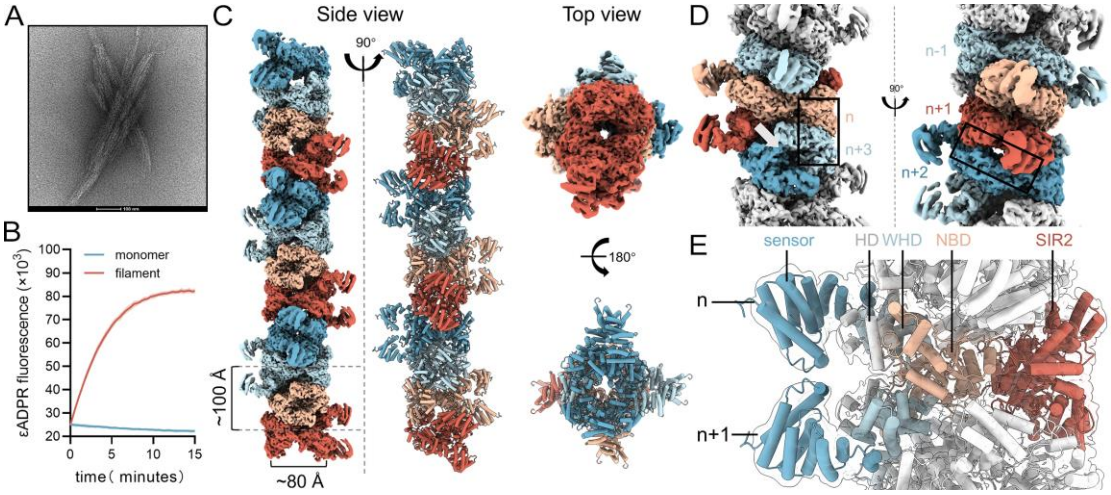


**Fig2. Cryo-EM structure of the *Ef*Avs5 filament.**

(**A**) Representative negative-stain micrograph images of *Ef*Avs5. The scale bar represents 100 nm. (**B**) *Ef*Avs5's NADase activity is activated by filamentation. After the addition of ε-NAD$^+$, total fluorescence was measured over time. Data represent the mean of three replicates and shaded regions represent the SEM. (**C**) Top and side views of the density map and the atomic model of *Ef*Avs5 filament. (**D**) Detailed view of *Ef*Avs5 filament to show the subunit interfaces. Two interfaces are indicated with boxes, and the NAD$^+$ active site is indicated with a grey arrow. (**E**) The core of *Ef*Avs5 filament is composed of the SIR2 domain and the NOD.

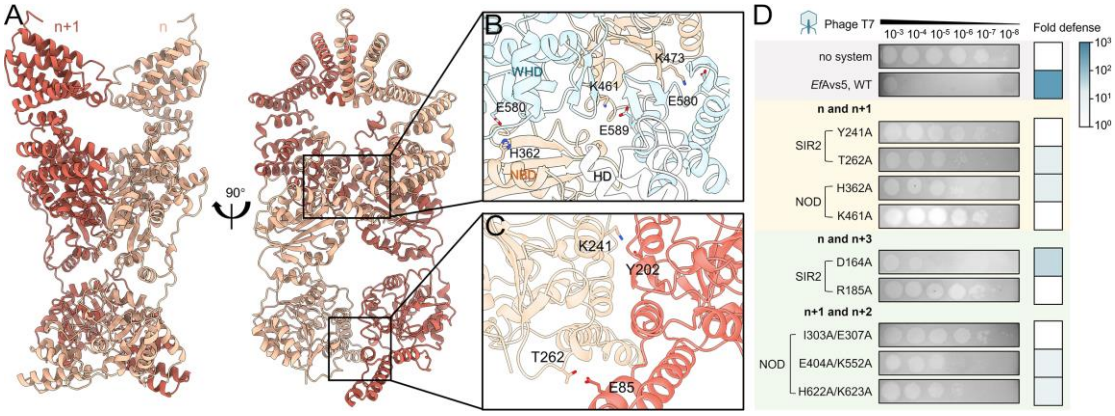


**Fig3. The mechanism of *Ef*Avs5 dimerization.**

(**A**) The structure of the *Ef*Avs5 dimer. (**B**) Details of the NOD-based dimeric interfaces. (**C**) Details of the SIR2-based dimeric interfaces. (**D**) Phage plaque assay of *E. coli* expressing *Ef*Avs5 variants with mutations at the interfaces. The yellow background highlights the intra-dimer interactions, while the green background indicates the inter-dimer interactions. Data are representative images of n=3 biological replicates.

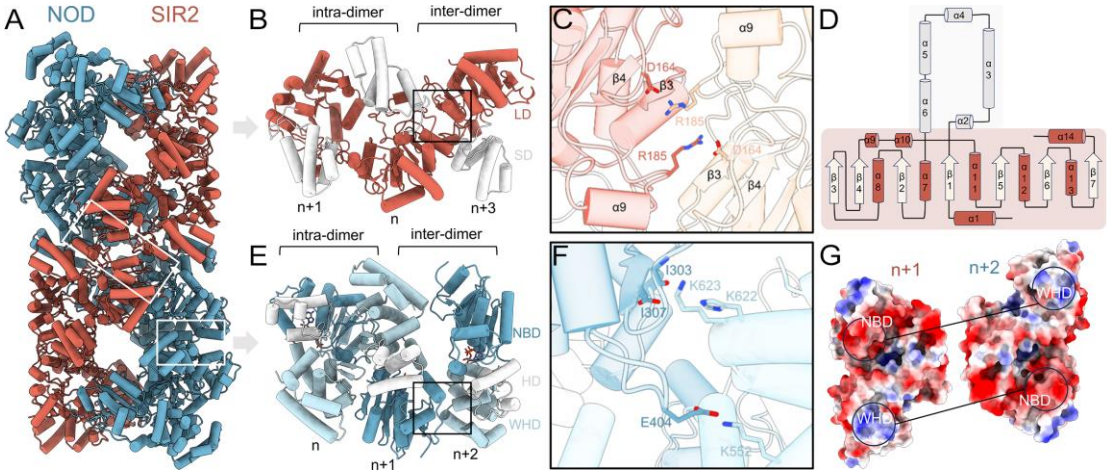


**Fig 4. SIR2- and NOD-dependent filamentation.**

(**A**)Two spirals dominated by NOD (blue) and SIR2 domains (red), respectively. The C-terminal domains of *Ef*Avs5 are hided. The inter-dimer interactions are indicated by white boxes. (**B**) The intra-dimer and inter-dimer interface of SIR2 domain of the n+1, n, n+3 subunits. LD, large domain; SD, small domain. (**C**) Detailed inter-dimer interface of SIR2 domain. The n, n+3 subunits of *Ef*Avs5 was colored red and orange, respectively. (**D**) SIR2 topology diagrams of *Ef*Avs5. The small domain is shaded grey, and the large domain is shaded red. (**E**) The intra-dimer and inter-dimer interface of NOD domain of the n, n+1, n+2 subunits. (**F**) Detailed inter-dimer interface of NOD domain. The NBD of n+1 subunit, and the WHD of n+2 subunit of *Ef*Avs5 were colored dark and light blue, respectively. (**G**) The electrostatic potential inter-dimer interface of two adjacent NOD domains.

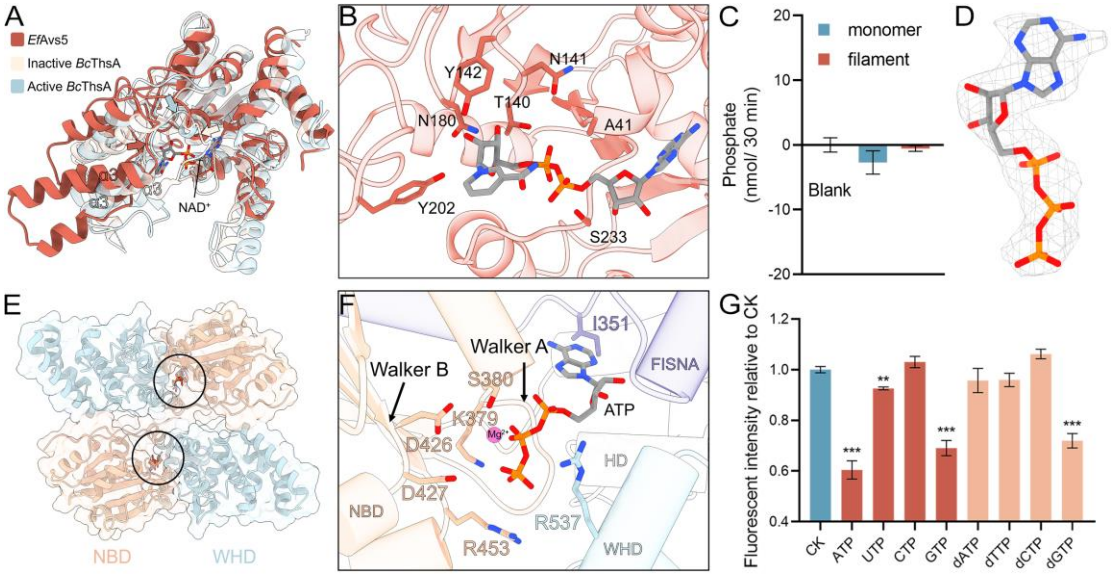


**Fig 5. The NAD⁺ hydrolyzing pocket and ATP binding pocket of *Ef*Avs5.**

(**A**) Overlay of SIR2 domain (red) of *Ef*Avs5 with the inactive (6LHX, light orange) and activated (light blue) *Bc*ThsA SIR2 domains. $NAD^+$ from the activated ThsA (1ICI) is shown. The loops above the $NAD^+$ pocket of *Ef*Avs5 and ThsA SIR2 are indicated by arrows colored as in the color scheme. (**B**) Residues of *Ef*Avs5 interacting with $NAD^+$ molecule highlighted in sticks in the predicted *Ef*Avs5-$NAD^+$ binding model. (**C**)ATPase activity assay of the monomer or the filament *Ef*Avs5. Data represent the mean of three replicates and error bars represent the SEM. (**D**) Cryo-EM map of ATP. (**E**) The binding pocket of ATP in the NOD dimer. (**F**) Residues of *Ef*Avs5 coordinating ATP molecule highlighted in sticks. The highly conserved Walker A motif and Walker B motif were indicated by arrows. (**G**) Effects of NTPs and dNTPs (5 mM) on NADase activity of the *Ef*Avs5. CK: no NTPs/dNTPs added. Data represent the mean of three replicates and error bars represent the SEM.

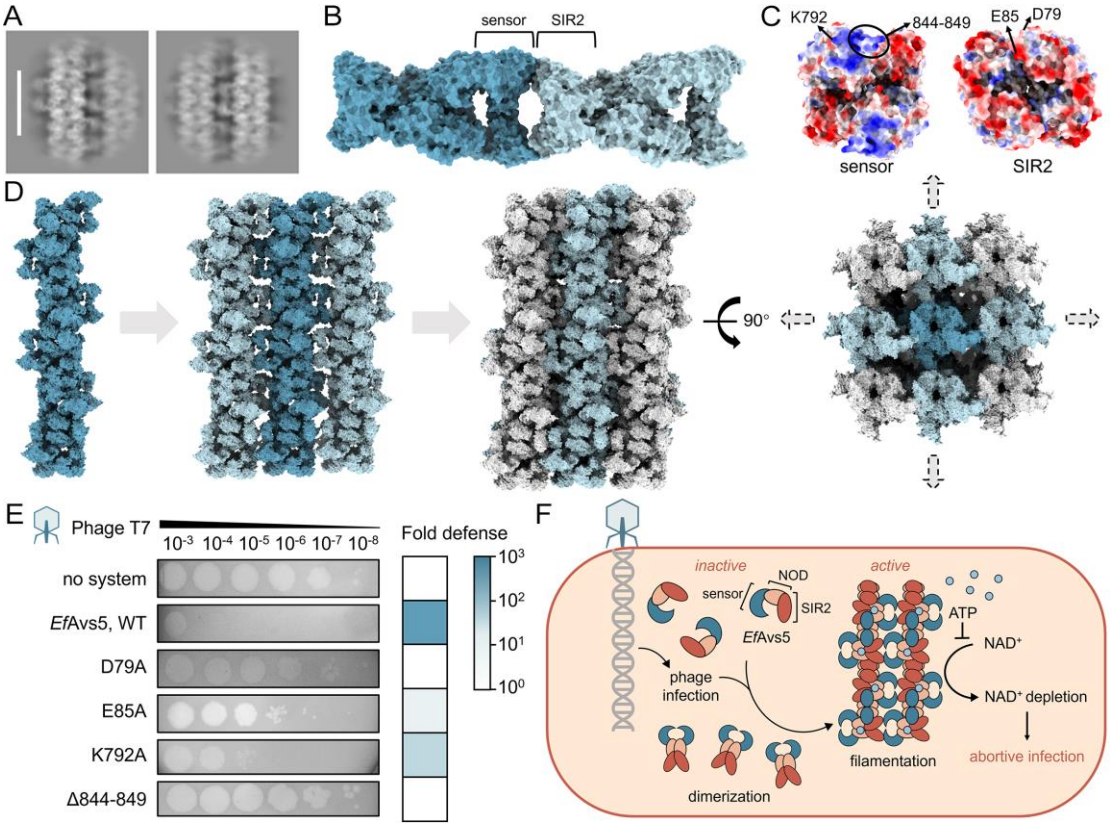


**Fig 6. Filamentous cluster formation mediates *Ef*Avs5 anti-phage activity**

(**A**) 2D class averages of the particle stacks, showing the bundled filament assembly. The scale bar represents 130 Å. (**B**) Interacting *Ef*Avs5 dimers in adjacent filaments. (**C**) The electrostatic potential interface of C-terminal sensor and N-terminal SIR2 domain. (**D**) A schematic diagram of the filament cluster assembly of *Ef*Avs5. (**E**) Phage plaque assay of *E. coli* expressing *Ef*Avs5 variants with mutations at the clustering interfaces. Data are representative images of n=3 biological replicates. (**F**) Proposed model of *Ef*Avs5 immune mechanism. Without phage infection, *Ef*Avs5 remains inactive as monomer. Phage infection activates *Ef*Avs5, forming filament bundles where SIR2 enable rapid $NAD^+$ degradation and aborting phage infection.